# Time-of-flight polarization contrast neutron imaging for enhanced characterization of ferritic phase fractions in Fe-Mn-Si shape memory alloys

**Matteo Busi**[1]**, Irene Ferretto** [2]**, Florencia Malamud**[1]**, Christian Leinenbach** [2]**, Markus Strobl**[1]

[1] Paul Scherrer Institut, Laboratory for Neutron Scattering and Imaging, 5232 Villigen, Switzerland
[2] Empa, Swiss Federal Laboratories for Materials Science and Technology, 8600 Dubendorf, Switzerland

E-mail: `matteo.busi@psi.ch`

**Abstract.** The determination of the amount and distribution of different phase fractions in additively manufactured shape memory alloys processed with laser powder bed fusion is crucial for understanding the correlation between processing parameters, microstructure, and mechanical properties. Neutron imaging techniques, such as Bragg edge imaging and polarization contrast neutron imaging (PNI), have been introduced to complement and overcome the limitations of traditional characterization methods, which are often destructive and limited to surface analyses and small-sized specimens. Bragg edge imaging can distinguish and quantify crystallographic phase fractions with spatial resolutions of a few tens of micrometers, while PNI is highly sensitive to crystallographic phases and is particularly suited for sub-percent phase fractions and in-situ, time-resolved, and tomographic analyses. In this work, we present a time-of-flight PNI method that enables simultaneous measurements of phase fractions.

## 1. Introduction

Fe-based shape memory alloys (SMAs) are a class of smart materials that can recover the original shape after significant deformation. The functional properties of SMAs strongly depend on microstructural features, e.g. texture, grain size, phase fraction [1]. Laser powder bed fusion (LPBF) is an additive manufacturing technique that allows for the manipulation of the microstructure of a build component. By varying the LPBF process parameters, components with tailored phase volume fractions, grain size and texture can be fabricated, as the thermal history in the deposited material can be site-specifically controlled and modified [2]. In a recent study [3], it has been demonstrated that the microstructure of a Fe-Mn-Si-based SMA could be varied in a rather wide range by simply changing the laser scan velocity during LPBF. Specifically, the volume phase fraction of the bcc-$\delta$ ferrite and fcc-$\gamma$ austenite phases could be tailored in the fabricated samples, showing an increase in material strength but a decrease in the shape memory properties with a higher amount of bcc-$\delta$. The determination of the amount and distribution of different phases in the LPBF fabricated samples is thus of primary importance to fully understand the existing correlation between processing parameters, microstructure and

mechanical properties of LPBF samples to apply LPBF as an effective tool for microstructure and properties manipulation.

Conventional techniques (e.g. optical microscopy, electron microscopy, electron backscatter diffraction, X-ray diffraction) are limited to small-sized samples and surface analyses and require destructive approaches to access bulk properties. The high penetration of neutrons in metallic specimens makes it an efficient probe to study bulk microstructural properties. In the last two decades, novel neutron imaging methods have been developed to gain spatially resolved insights to meso-scale phenomena in the bulk of polycrystalline materials, useful, in particular, for complex sample geometries enabled through additive manufacturing. One of these techniques, Bragg edge imaging (BEI) [4, 5], has shown the capability to quantitatively map phase distributions both in radiographic and tomographic mode [6, 7, 8, 9] and to reveal the phase evolution [10, 11, 12] with spatial resolutions down to a few tens of μm. However, since this method relies on accurate determination of the wavelength spectrum of the attenuation coefficient it is often challenged by spectral distortions due to the presence of crystallographic texture or other microstructural properties, and requires a relatively high exposure time to achieve a suitable signal to noise ratio. Another neutron imaging technique that has raised interest in the last two decades is polarization contrast neutron imaging (PNI) [13]. For certain applications, in particular for depolarization contrast, it can be carried out with a white beam, thus, exploiting high flux capabilities. Depolarization contrast provides information about the content of non-parallel magnetic field components with respect to the initial polarization in a sample system. Such approach was used in the past for example to map phase transitions from the paramagnetic to ferromagnetic at the Curie temperature of a PdNi crystal [14] or to visualize trapped magnetic field in a bulk YBCO superconductor at different temperatures below the Curie temperature [15]. In a recent study, it was shown that using PNI, it is possible to reveal and quantify magnetic crystallographic phases in iron-based materials [16]. The method is in particular efficient to identify small phase fractions with high spatial resolution and short exposure times, making it an efficient tool for tomographic and in-situ time-resolved studies. However, the method is only sensitive to the interactions between the neutron and the magnetic field present in the sample and thus, one has to make assumptions or separate measurements to determine the corresponding crystal structure. In addition, high phase fractions may depolarize the neutron beam completely hindering accurate quantitative analyses.

Here we introduce an advanced approach that combines BEI and PNI in a simultaneous multi-modal time-of-flight measurement of the attenuation and the depolarization of a polarized neutron beam following the passage through the investigated sample. The method is applied to study the presence of magnetic phases in additively manufactured Fe-Mn-Si SMAs processed through LPBF with different laser speeds. While PNI provides an efficient tool for mapping locally especially small ferritic phase fractions with high spatial resolution, BEI complements it with the determination of the specific crystal structures and its sensitivity to high phase fractions.

## 2. Methods and experiments

A time-of-flight polarization contrast neutron imaging (TOF-PNI) measurement consists of a set of two exposures of the wavelength- and spatially- resolved spin-*up* intensity $I_\uparrow(x, y, \lambda)$ and spin-*down* intensity $I_\downarrow(x, y, \lambda)$, recorded subsequently utilizing an adiabatic fast passage $\pi$ spin flipper. The local total intensity of the beam is obtained by summing up the two spin-state intensities:

$$I(x, y, \lambda) = I_\uparrow(x, y, \lambda) + I_\downarrow(x, y, \lambda), \tag{1}$$

while the local polarization of the beam is obtained according to the ratio:

$$P(x,y,\lambda) = \frac{I_\uparrow(x,y,\lambda) - I_\downarrow(x,y,\lambda)}{I_\uparrow(x,y,\lambda) + I_\downarrow(x,y,\lambda)}. \tag{2}$$

The procedure is repeated with and without the sample, to allow for open beam normalization of beam intensity and beam polarization, and the analysis of the neutron interactions with the investigated specimens. The Beer-Lambert law of attenuation is used to calculate the linear attenuation coefficient spectrum:

$$\mu(x,y,\lambda) = -\frac{1}{t(x,y)} \log \frac{I(x,y,\lambda)}{I_0(x,y,\lambda)}, \tag{3}$$

where $I_0$ is the incident beam intensity, $I$ is the transmitted beam intensity and $t$ is the sample thickness. For a polycrystalline material with a large coherent cross section the linear attenuation coefficient spectrum is characterized by so-called Bragg edges, occurring at wavelengths $\lambda = 2d_{\mathrm{hkl}}$ corresponding to specific families of lattice planes (hkl) according to the crystal structure. Bragg's law relates the neutron wavelength $\lambda$ to the Bragg angle $\theta$ between the beam and the lattice planes as

$$\lambda = 2d_{\mathrm{hkl}} \sin(\theta), \tag{4}$$

where $d_{\mathrm{hkl}}$ is the lattice spacing. Bragg edges in transmission occur accordingly at $\theta = 90°$. The analysis of the full pattern of the Bragg edges for different (hkl) lattice planes in each pixel of the imaging detector allows the discrimination of individual crystal structures or to reveal and quantify crystalline phases and phase transformations in materials. Furthermore, the wavelength of specific Bragg edges can be tracked across the sample volume to extract lattice strain maps, for the strain direction parallel to the neutron beam. Finally, from the shape of the spectra and of Bragg edges, one can in principle deduce microstructural material property information such as related to crystallite size and crystallographic texture.

In addition to the beam attenuation, when a polarized neutron beam passes through a ferromagnetic material, the neutron spins undergo Larmor precessions with the frequency $\omega_L = \gamma\mathbf{B}$, depending on the neutron wavelength and according to the strength and orientation of the magnetic field $\mathbf{B}$ of magnetic domains. $\gamma = 4\pi\mu_n/h$ is the gyromagnetic factor of the neutron with $h$ being the Planck constant [17]. Assuming a random distribution of domain orientations, the depolarization depends on $\mathbf{B}$, the average domain size $d$ and sample thickness as well as on the neutron velocity $\nu$, i.e. wavelength. In analogy to the Beer Lambert law of attenuation, one can write the depolarization coefficient $\eta$ in a first approximation:

$$\eta(x,y,\lambda) = -\frac{1}{t(x,y)} \log \frac{P(x,y,\lambda)}{P_0(x,y,\lambda)}, \tag{5}$$

for a ferromagnetic material with randomly oriented domains as expressed by Halpern and Holstein [18] as:

$$\eta = \frac{\gamma^2 \mathbf{B}^2 d}{3\nu^2} = \frac{1}{3}\left(\frac{4\pi\mu_n\lambda m}{h^2}\mathbf{B}\right)^2 d. \tag{6}$$

The latter is used in this work to quantify phase fractions of ferromagnetic domains of ferrite in the paramagnetic phase matrix not interfering with the neutron spin.

The experiments were conducted at the BOA [19] beamline at SINQ (PSI, Switzerland). The setup is similar to the one used previously [16], with the addition of a chopper to enable TOF measurements, as is sketched in Fig. 1. The beam is polarized by a multichannel polarizing-bender unit, which at BOA is permanently installed upstream of the collimation
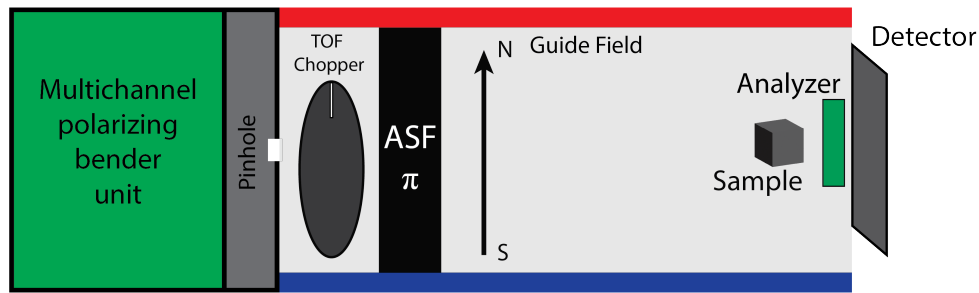
**Figure 1.** Instrumentation setup sketch for time-of-flight polarization contrast neutron imaging at BOA.

pinhole. A magnetic guide field of approximately 5.2 mT is mounted throughout the beamline to preserve the polarization of the neutron beam. A fast adiabatic spin flipper (ASF) enables a $\pi$ rotation of the neutron spins, which are analyzed by an additional spin filter with an active area of $40 \times 40$ mm$^2$ mounted in front of the detector. To enable efficient time-of-flight (TOF) measurements, we used a chopper disk, such as the one used for frame overlap Bragg edge imaging (FOBI) [20], with three pseudorandom slit pattern of 14 rectangular slits, each with a width of 1.8 mm. The pattern is repeated identically in three sections of the chopper disk, such to have a suitable wavelength range at a rotation frequency of 25 Hz. The detector system consisted of a 100 μm 6LiF:ZnS scintillator positioned in the direct beam, a mirror positioned at 45° relative to the scintillator, a focusing lens to adjust the focus onto the scintillator surface, an MCP image intensifier, and the ASI optical camera TPX3Cam based on a Timepix3 chip [21]. The final optical setup produced a field-of-view of $10 \times 10$ cm$^2$, with an effective pixel size of 90 μm. The detector was set approximately 6 m away from the chopper, which resulted, considering the slit width, disk radius (200 mm) and rotation frequency, in a wavelength resolution $\Delta\lambda/\lambda = 1\%$ at $\lambda = 4$ Å.

The material studied in this work is an Fe-based SMA with the nominal composition Fe–17Mn–5Si–10Cr–4Ni-1(V,C) (wt. %) from previous studies reported in Refs [3, 22]. The powder was produced by gas atomization in Ar atmosphere (Boehler Edelstahl, Kapfenberg, Austria) and is characterized by spherical particles with a radius of 33 μm and a size distribution between 22 and 48 μm. The samples produced from the powder were fabricated in parallelepiped shape of $10 \times 10$ mm$^2$ and were cut via electro-discharge machining to have 3 mm height along the build direction. The specimens were manufactured in an Argon environment (less than 0.1% Oxygen content) using a Sisma MySint 100 (Sisma S.p.A., Italy) operating in continuous mode with a 1070 nm fiber-laser and a Gaussian intensity distribution with 55 μm spot size. A bidirectional scanning strategy with a 90° rotation between layers and border contour was applied for all the samples. Laser processing parameters such as laser power, hatch distance and powder layer thickness were kept fixed to 175 W, 100 μm and 30 μm, respectively. However, to achieve different volumetric energy density (VED) and thus, different ferrite bcc-$\delta$ phase fractions, the samples were processed with different laser speeds, listed in Table 1. The ferrite phase fraction used as reference was measured with a Fisher feritscope FMP30®. Note that even though the ferrite phase fraction should scale with the laser speed, feritscope measurements lead to similar values for the samples 2 and 3 due to manufacturing issues, as will be revealed by the PNI measurements in the next section.

**Table 1.** Specimens measured and respective laser speed, VED and ferrite phase fraction.

| Sample label | Speed (mm/s) | VED (J/mm$^3$) | Ferrite (%) |
|---|---|---|---|
| 1 | 300 | 194.4 | 36.4 |
| 2 | 400 | 145.8 | 6.8 |
| 3 | 500 | 116.7 | 7.9 |
| 4 | 600 | 97.2 | 3.2 |

## 3. Results

Figure 2 shows plots of the open beam intensity and polarization as a function of neutron wavelength. The conversion from TOF to wavelength was performed via calibration with a
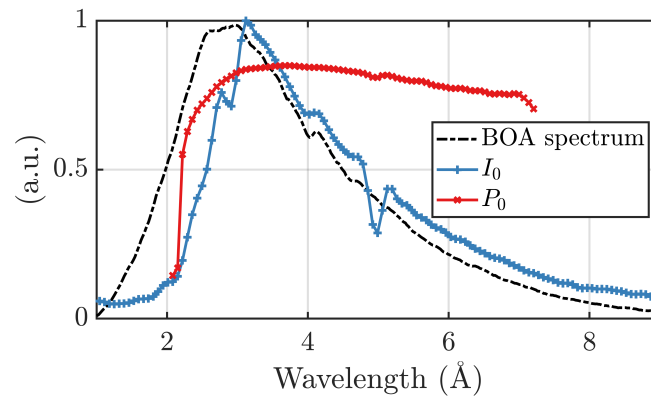


**Figure 2.** Open beam intensity and polarization spectra.

reference iron powder, using Bragg edge wavelengths of well-known lattice planes. It is observed that Bragg dips are present in the beam spectrum, at 3.0 and 5.1 Å, due to the coated mirror blades present in the spin analyzer however, as discussed below, they don't seem to influence the measured transmission spectra of the samples as the dip features disappear following the open beam normalization (note that both sample and open beam measurements were taken with the spin analyzer installed). Furthermore, the spin analyzer was designed to have a cutoff wavelength of approximately 2.2 Å. Therefore, Bragg edge imaging applications are prohibited for shorter wavelengths with the utilized spin analyzer. However, the latter could be designed and constructed such to allow transmission at different wavelength ranges. Consequently, the measured polarization sharply rises up from the cutoff wavelength to a maximum polarization of 85.0% at 3.8 Å and slowly decreases with longer wavelengths. A polarization higher than 70.0%, which seems to be sufficient for polarization analyses as shown in the next section, is satisfied for wavelengths above 2.5 Å.

The field of view enabled by the spin analyzer allowed to measure four specimens within a single radiographic exposure. The batch of samples measured was chosen to be in a suitable range of ferrite phase fraction for quantitative characterization through both PNI and BEI. It consists of four samples labeled from 1 to 4 in Table 1, each with a height (build direction) of 3 mm aligned to the beam direction. Figure 3 shows the wavelength integrated transmission map of the samples, where only attenuation contrast contributes, thus revealing only bulk density

inhomogeneities within the sample volume, and averaged Bragg edge patterns of the four different samples (Fig. 3b). A higher ferrite phase fraction in a sample corresponds to the increase of attenuation in the proximity of wavelengths related to the $(110)_{bcc}$ lattice planes of the ferritic phase. Furthermore, it is observed that even for the sample 4, which only accounts to a 3% ferrite phase fraction, the typical Bragg edge occurring for the $(111)_{fcc}$ lattice planes of the austenite is suppressed due to the presence of crystallographic texture strongly oriented parallel to the $(200)_{fcc}$ lattice planes, which in turns yield a strong Bragg edge contrast. This type of crystallographic texture could be confirmed by separate electron back-scatter diffraction (EBSD) measurements [3].
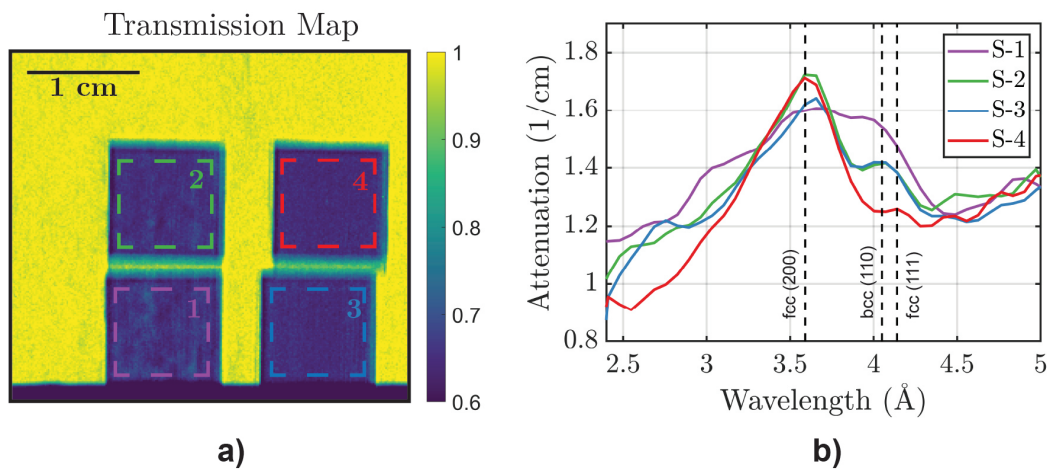


**Figure 3.** a) White beam transmission map of the four samples measured. b) Average attenuation $(cm^{-1})$ Bragg patterns of the four samples for the bulk region of interest indicated in a). The color code of the plotted lines matches the marked regions of interest in the transmission map.

With respect to the PNI, the quantitative determination of ferrite phase fraction was carried out with a procedure similar to the one reported in [16]. In a first approach, all the TOF frames were integrated to achieve synthetic white beam data sets for the spin-up and spin-down configurations, both for the sample and the open beam measurements. The white beam depolarization map was calculated and converted to linear depolarization map by correcting for the sample thickness. From the latter, the ferrite phase fraction map was obtained by calibrating to the reference phase fraction of sample 4 measured with the feritscope. Figure 4 shows the ferrite phase fraction map of the four samples measured. It is clearly seen that the bcc-$\delta$ phase is not uniformly distributed through the sample volume, which is highlighted in the horizontal line profiles. It is observed for samples 3 and 4 that a region, both visible in the maps and in the horizontal line profiles, in the middle of the sample yields a higher phase fraction. Sample 2, which yields similar ferritic fractions as sample 3 by the feritscope reading, likely due to the large gauge volume of the probe used, is the one that exhibits the strongest phase fraction contrast within its sample volume. It rises from a region with average 4% ferrite at the top of the sample, to an inner region of maximum average phase fraction accounting to approximately 15%. The reason of this inhomogeneity is found in the heat accumulation caused by the fact that the laser is always moving from the top-side of the samples to the bottom-side within the same layer. Sample 1 reveals a homogeneous map of approximately 20% ferrite phase fraction that due to a complete depolarization of the beam by the sample results in a depolarization
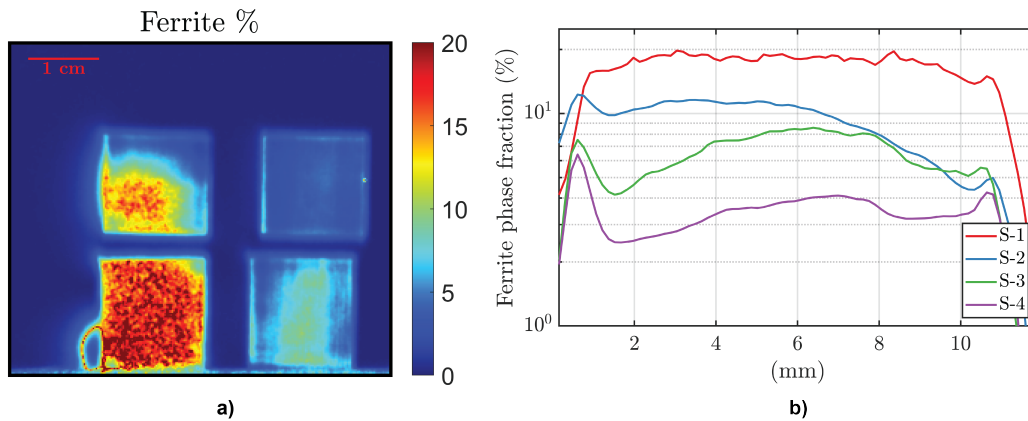
**Figure 4.** a) Ferrite phase fraction (%) maps obtained through white beam PNI measurements. b) Horizontal averaged line profiles for the bulk sample regions of interest indicated in Fig. 3a.

ratio approaching zero (Fig. 6). Thus, it can be stated that white beam polarization contrast imaging fails to characterize quantitatively such a high phase fraction of magnetic phase.

Additionally, a spatially resolved phase fraction map could not be extracted by means of Bragg edge imaging for this experiment, due to the high exposure required by this modality to achieve suitable signal statistics. Nonetheless, the average bulk phase fraction of each sample could be calculated from the region of interest Bragg patterns shown in Fig. 3b, using a fitting procedure similar to the one reported in [8], which takes into account for the presence of texture. Figure 5 shows a plot of the average bulk phase fraction values of the different samples measured with the two multi-modal approaches (i.e. Bragg edge imaging and white beam PNI) enabled by the TOF-PNI technique presented in this manuscript. The values are plotted versus their
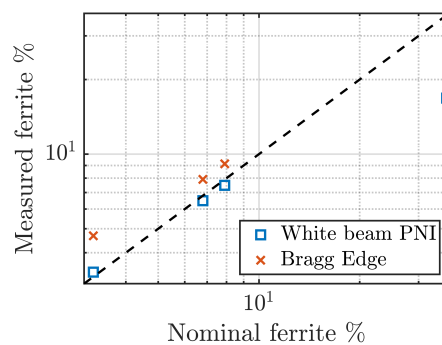


**Figure 5.** Comparison of the ferrite phase fraction quantification as measured through white beam PNI (square markers) and BEI (cross markers). The black-dashed line represents the reference trend according to feritscope measurements.

corresponding reference values measured with the feritscope. It can be observed that while the white beam PNI approach provides the most accurate values for phase fractions below 10%, it fails to quantitatively characterize sample 1, due to the complete depolarization of the beam by the high ferrite fraction. In turn, such a high phase fraction is efficiently extracted through Bragg edge imaging, which however decreases in accuracy as the phase fraction decreases leading to a

maximum discrepancy for sample 4. We note that PNI does not distinguish between different crystallographic structures, but is only sensitive to ferromagnetic phases with magnetic domains (as is the case for ferrite bcc-$\delta$), whereas through BEI it is possible to discriminate between different crystal structures. On the other hand, the quantification of magnetic phase fraction through BEI is challenged by other microstructural properties of the specimens affecting the Bragg edge pattern such as crystallographic texture, grain size etc.

Yet another aspect to consider for the multi-modal approach presented here is the wavelength dependence of the depolarization. Figure 6 shows the average bulk depolarization ratio of the four samples as function of the neutron wavelength, measured through TOF-PNI. It is observed,
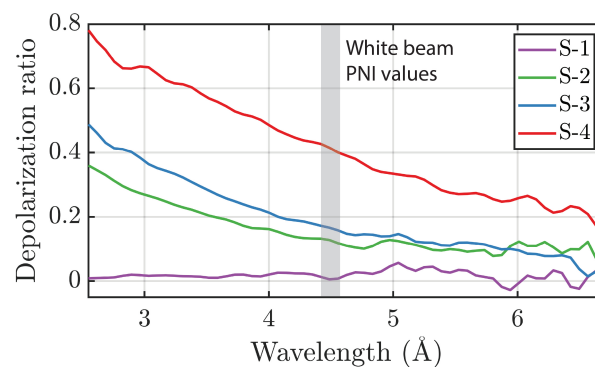


**Figure 6.** Average bulk depolarization ratio as function of neutron wavelength of the four samples measured. The gray box indicates the wavelength interval corresponding to the values probed in white beam configuration.

that the depolarization increases as a function of wavelength, corresponding to Eq. 6 [18]. A grey vertical stripe in the graph marks the wavelength of approximately for 4.5 Å for which the depolarization corresponds to that of a white beam depolarization measurement with the spectrum of BOA . While for the samples considered in this manuscript, this aspect does not impact quantification even utilizing the white beam depolarization contrast, it highlights that a wider range of phase fractions can be quantified by depolarization imaging by varying the wavelength. Shorter wavelengths enable the quantification of higher phase fractions, while longer wavelengths increase the sensitivity to smaller phase fractions. Thus, a wavelength selective approach using e.g. a velocity selector or a double crystal monochromator, and a design of spin analyzer optimized for a wide range of neutron wavelengths increases the dynamic range of this imaging method, at the expense of measurement time and thus time resolution.

## 4. Conclusions

We have presented a multi-modal approach for the quantitative determination of magnetic crystallographic phases, which takes advantage of the complementary strengths of Bragg edge and polarization contrast imaging. It is discussed how the interdependency of two imaging modalities compensates for their individual limitations, not only by expanding the quantitative capability and accuracy to a broader range of e.g. ferrite phase fractions, but also in achieving an overall better understanding of the structural properties of the investigated specimens. The wavelength dependence of the neutron beam depolarization induced by ferromagnetic phases in the sample is found to enable tailoring the sensitivity to the needs of specific measurements overcoming limitations of white beam depolarization imaging at the expense, however, of time resolution.

## Acknowledgments

## References

[1] Cladera, Antoni, et al. "Iron-based shape memory alloys for civil engineering structures: An overview." *Construction and building materials* **63** (2014): 281-293.

[2] DebRoy, Tarasankar, et al. "Additive manufacturing of metallic components–process, structure and properties." *Progress in Materials Science* **92** (2018): 112-224.

[3] Ferretto, Irene, et al. "Control of microstructure and shape memory properties of a Fe-Mn-Si-based shape memory alloy during laser powder bed fusion." *Additive Manufacturing Letters* **3** (2022): 100091.

[4] Santisteban, J. R., et al. "Time-of-flight neutron transmission diffraction." *Journal of applied crystallography* **34.3** (2001): 289-297.

[5] Woracek, Robin, et al. "Diffraction in neutron imaging—A review." *Nuclear Instruments and Methods in Physics Research Section A: Accelerators, Spectrometers, Detectors and Associated Equipment* **878** (2018): 141-158.

[6] Woracek, Robin, et al. "3D Mapping of Crystallographic Phase Distribution using Energy-Selective Neutron Tomography." *Advanced Materials* **26.24** (2014): 4069-4073.

[7] Makowska, Malgorzata G., et al. "Investigating phase behavior and structural changes in NiO/Ni-YSZ composite with monochromatic in-situ 2D and static 3D neutron imaging." *Physica B: Condensed Matter* **551** (2018): 24-28.

[8] Polatidis, Efthymios, et al. "Neutron diffraction and diffraction contrast imaging for mapping the TRIP effect under load path change." *Materials* **13.6** (2020): 1450.

[9] Sato, Hirotaka, et al. "Relation between Vickers hardness and Bragg-edge broadening in quenched steel rods observed by pulsed neutron transmission imaging." *Materials Transactions* **56.8** (2015): 1147-1152.

[10] Makowska, Małgorzata G., et al. "In situ time-of-flight neutron imaging of NiO–YSZ anode support reduction under influence of stress." *Journal of Applied Crystallography* **49.5** (2016): 1674-1681.

[11] Makowska, Malgorzata Grazyna, et al. "Coupling between creep and redox behavior in nickel-yttria stabilized zirconia observed in-situ by monochromatic neutron imaging." *Journal of Power Sources* **340** (2017): 167-175.

[12] Dabah, Eitan, et al. "Time-resolved Bragg-edge neutron radiography for observing martensitic phase transformation from austenitized super martensitic steel." *Journal of Materials Science* **52.6** (2017): 3490-3496.

[13] Strobl, M., et al. "Advances in neutron radiography and tomography." *Journal of Physics D: Applied Physics* **42.24** (2009): 243001.

[14] Schulz, Michael, et al. "Towards a tomographic reconstruction of neutron depolarization data." *Journal of Physics: Conference Series* **211** (2010).

[15] Kardjilov, Nikolay, et al. "Advances in neutron imaging." *Materials Today* **21.6** (2018): 652-672.

[16] Busi, M., et al. "Polarization contrast neutron imaging of magnetic crystallographic phases." *Materials Today Advances* **16** (2022): 100302.

[17] Strobl, M., et al. "Polarization measurements in neutron imaging." *Journal of Physics D: Applied Physics* **52.12** (2019): 123001.

[18] Halpern, O., and T. Holstein. "On the passage of neutrons through ferromagnets." *Physical Review* **59.12** (1941): 960.

[19] Morgano, M., et al. "Neutron imaging options at the BOA beamline at Paul Scherrer Institut." *Nuclear Instruments and Methods in Physics Research Section A: Accelerators, Spectrometers, Detectors and Associated Equipment* **754** (2014): 46-56.

[20] Busi, M., et al. "Frame overlap Bragg edge imaging." *Scientific Reports* **10.1** (2020): 1-10.

[21] Losko, A. S., et al. "New perspectives for neutron imaging through advanced event-mode data acquisition." *Scientific reports* **11.1** (2021): 1-11.

[22] Ferretto, I., et al. "Shape recovery performance of a (V, C)-containing Fe–Mn–Si–Ni–Cr shape memory alloy fabricated by laser powder bed fusion." *Journal of Materials Research and Technology* **20** (2022): 3969-3984.